Article

Observation of Proton Transfer Coupled Spin Transition and Trapping of Photoinduced Metastable Proton Transfer State in an Fe(II) Complex

Takumi Nakanishi, Yuta Hori, Hiroyasu Sato, Shuqi Wu, Atsushi Okazawa, Norimichi Kojima, Takashi Yamamoto, Yasuaki Einaga, Shinya Hayami, Yusuke Horie, Hajime Okajima, Akira Sakamoto, Yoshihito Shiota, Kazunari Yoshizawa, and Osamu Sato

J. Am. Chem. Soc., **Just Accepted Manuscript** • DOI: 10.1021/jacs.9b07204 • Publication Date (Web): 17 Aug 2019

Observation of Proton Transfer Coupled Spin Transition and Trapping of Photoinduced Metastable Proton Transfer State in an Fe(II) Complex.

Takumi Nakanishi[1], Yuta Hori[1,2], Hiroyasu Sato[3], Shuqi Wu[1] Atsushi Okazawa[4], Norimichi Kojima[5], Takashi Yamamoto[6], Yasuaki Einaga[7], Shinya Hayami[7,8], Yusuke Horie[9], Hajime Okajima[9], Akira Sakamoto[9], Yoshihito Shiota[1], Kazunari Yoshizawa[1], and Osamu Sato[1*]

[1]Institute for Materials Chemistry and Engineering & IRCCS, Kyushu University, 744 Motooka, Nishi-ku, Fukuoka 819-0395, Japan.

[2]Center for Computational Sciences, University of Tsukuba, Tsukuba 305-8577, Japan.

[3]Rigaku Corporation, 3-9-12 Matsubaracho, Akishima, Tokyo 196-8666, Japan.

[4]Department of Basic Science, Graduation School of Arts and Sciences, The University of Tokyo, 3-8-1 Komaba, Meguro-ku, Tokyo 153-8902, Japan.

[5]Toyota Physical and Chemical Research Institute, Yokomichi, Nagakute, Aichi 480-1192, Japan.

[6]Department of Chemistry, Faculty of Science and Technology, Keio University, 3-14-1 Hiyoshi, Kohoku-ku, Yokohama, Kanagawa 223-8522, Japan.

[7]Department of Chemistry, Faculty of Advanced Science and Technology, Kumamoto University, 2-39-1 Kurokami, Chuo-ku, Kumamoto 860-8555, Japan.

[8]Institute of Pulsed Power Science (IPPS), Kumamoto University, 2-39-1 Kurokami, Chuo-ku, Kumamoto 860-8555, Japan.

[9]Graduate School of Science and Engineering, Aoyama Gakuin University, 5-10-1 Fuchinobe, Chuo-ku, Sagamihara, Kanagawa 252-5258, Japan.

KEYWORDS (Word Style "BG_Keywords"). Proton Transfer; Spin transition;

ABSTRACT: An important technique to realize novel electron- and/or proton-based functionalities is to use a proton–electron coupling mechanism. When either a proton or electron is excited, the other one is modulated, producing synergistic functions. However, although compounds with proton-coupled electron transfer have been synthesized, crystalline molecular compounds that exhibit proton-transfer-coupled spin-transition (PCST) behavior have not been reported. Here, we report the first example of a PCST Fe(II) complex, wherein the proton lies on the N of hydrazone and pyridine moieties in the ligand at high-spin and low-spin Fe(II), respectively. When the Fe(II) complex is irradiated with light, intramolecular proton transfer occurs from pyridine to hydrazone in conjunction with the photoinduced spin transition via the PCST mechanism. Because the light-induced excited high-spin state is trapped at low temperatures in the Fe(II) complex—a phenomenon known as the light-induced excited-spin-state trapping effect—the light-induced proton-transfer state, wherein the proton lies on the N of hydrazone, is also trapped as a metastable state. The proton transfer was accomplished within 50 ps at 190 K. The bistable nature of the proton position, where the position can be switched by light irradiation, is useful for modulating proton-based functionalities in molecular devices.

INTRODUCTION

Numerous functional compounds have been synthesized to develop electronic and protonic devices [1, 2]. One of the important routes to realize novel properties in solid-state materials is to couple two or more components. Indeed, various intriguing coupled systems, or cross-correlation systems, have been developed. They include the coupling of electron and proton transfer and the coupling of electric and magnetic dipole moments [3, 4]. An important characteristic of coupled systems is that, when one of the components is excited via external stimuli, the properties of the other coupled components are also modulated, thereby demonstrating coupling and concerted effects [5]. Indeed, various synergistic properties have been reported. Proton-coupled electron transfer, an example of a proton–electron coupling system, is well known to play an important role in biological systems [6]. Proton–electron coupling in solid-state materials, 1,5-dihalo-2,6-naphthoquinhydrones, has also been demonstrated [7]. More recently, several solid-state molecular compounds exhibiting proton–electron coupling have been reported [8-10]. However, although spin and charge are two important characteristics of electrons, no previous study has succeeded in demonstrating proton-transfer-coupled spin-transition (PCST) behavior in a crystalline molecular material. The successful coupling of proton transfer and spin transition will lead to the realization of various coupling properties. In particular, because

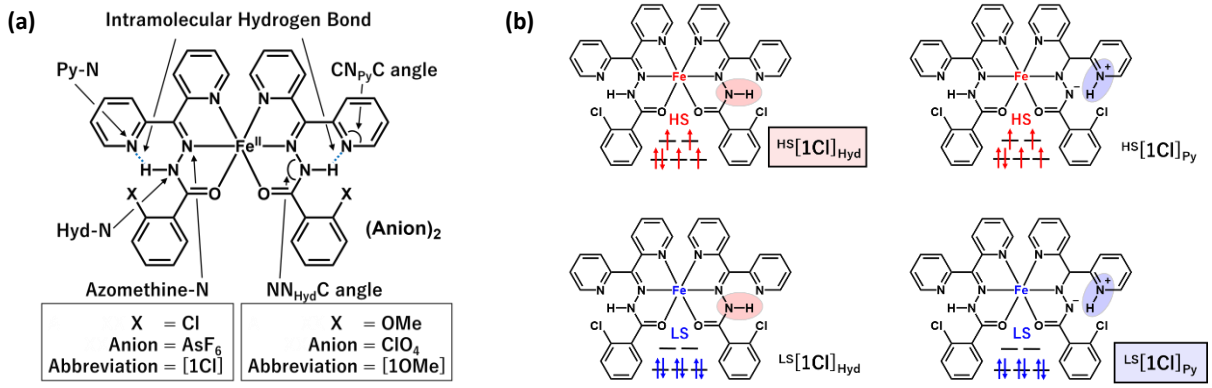

Figure 1. (a) Chemical structure of Fe(II) hydrazone complexes containing two *N*′-(di(pyridin-2-yl)methylene) benzohydrazide (HL) ligands. The HL ligands in which X is Cl and OMe are designated as HL-Cl and HL-OMe, respectively. Abbreviations of Fe(II) complexes bearing HL-Cl ($[Fe(HL\text{-}Cl)_2](AsF_6)_2$) and HL-OMe ($[Fe(HL\text{-}OMe)_2](ClO_4)_2$) are **[1Cl]** and **[1OMe]**, respectively. (b) Abbreviations for the four combinations of spin state and proton position ($^{\text{Spin state}}$**[1Cl]**$_{\text{Proton position}}$) and a schematic of their structure.

a spin transition is known to be induced by light and because a metastable excited high-spin state can be trapped at low temperatures (light-induced excited-spin-state trapping, LIESST), the compounds that demonstrate PCST behavior will undergo photoinduced proton transfer and photoinduced excited-proton-transfer-state trapping via the coupling mechanism.

In view of the aforementioned background information, we attempted to synthesize an Fe(II) complex as the first example of a crystalline material that exhibits PCST behavior. We then aimed to achieve photocontrol of proton transfer and the trapping of a photoinduced metastable proton-transfer state via the PCST mechanism. Here, we describe thermal- and photoinduced PCST and the trapping of a photoinduced metastable proton-transfer state in an Fe(II) complex, $[Fe(HL\text{-}Cl)_2](AsF_6)_2$ (**[1Cl]**) (HL-Cl = *N*′-(di(pyridin-2-yl)methylene)-2-chlorobenzohydrazide).

The present study is organized such that the first part of the manuscript documents PCST behavior in **[1Cl]** and later sections include discussions of photoinduced PCST and the trapping of the photoinduced PCST. To strengthen the validity of our interpretation of the experimental results, we synthesized an additional compound for comparison: $[Fe(HL\text{-}OMe)_2](ClO_4)_2$ (**[1OMe]**) (HL-OMe = *N*′-(di(pyridin-2-yl)methylene)-2-methoxybenzohydrazide). As opposed to **[1Cl]**, **[1OMe]** exhibits a spin transition without proton transfer (a proton-uncoupled spin transition). The analytical properties of the reference sample, except for the IR data, are given in the supplementary information and support the PCST behavior of **[1Cl]**.

RESULTS AND DISCUSSION

Molecular design for proton-transfer-coupled spin transition (PCST). To realize PCST and photoinduced proton transfer, we focused on an Fe(II) complex bearing hydrazone-type ligands that can form intramolecular hydrogen bonds. Hydrazone derivatives have been used to develop various functional molecules in which proton dynamics such as proton relay are observed[11-14]. In addition, Fe(II) complexes with NNO-type hydrazone ligand exhibit spin transition [15-23]. We designed an Fe(II) complex with a ligand of *N*′-(di(pyridin-2-yl)methylene)-benzohydrazide (HL) derivative, where the HL possesses a hydrazone group and a pyridine ring (Fig. 1(a)). The HL can form an intramolecular hydrogen bond between the N site in the pyridine ring (Py-N) and the N site in the hydrazone moiety (Hyd-N) even while forming a metal complex (Fig. 1(a))[24-27]. The Py-N and Hyd-N–H in hydrazone can act as proton acceptor and proton donor sites, respectively. Furthermore, the ligand field of HL on an Fe(II) ion is within the spin-transition region. Therefore, spin transition in Fe(II) can potentially couple to the proton transfer between Py-N and Hyd-N; the change in spin state in Fe(II) would influence the basicity of the proton acceptor and donor sites, and the proton transfer would affect the ligand field strength of the Fe(II) center. Furthermore, some Fe(II) spin-transition complexes that contain hydrazone-type ligands have been reported to exhibit the effects of LIESST [19-22]. Therefore, we synthesized Fe(II) complexes with HL derivative ligands, i.e., **[1Cl]** and **[1OMe]** (Fig. 1(a)). The correlation of abbreviations (Py-N, Hyd-N, azomethine-N, $NN_{Hyd}C$ angle, and $CN_{Py}C$ angle) frequently used in the text and the corresponding sites in **[1Cl]** and **[1OMe]** are shown in Fig. 1(a). The correlation of the four notations ($^{\text{Spin-State}}$**[1Cl]**$_{\text{Proton-Position}}$: $^{\text{HS}}$**[1Cl]**$_{\text{Hyd}}$, $^{\text{HS}}$**[1Cl]**$_{\text{Py}}$, $^{\text{LS}}$**[1Cl]**$_{\text{Hyd}}$, $^{\text{LS}}$**[1Cl]**$_{\text{Py}}$) and the four molecular structures bearing the information of their spin state and proton position are shown in Fig. 1(b).

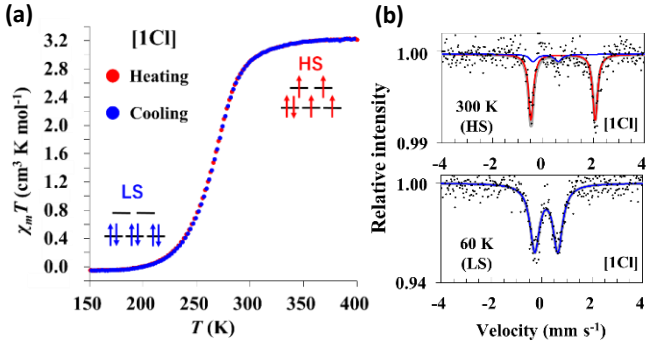

Figure 2. (a) $\chi_m T$–T plot for **[1Cl]**. (b) Mössbauer spectra of **[1Cl]**; (red line) HS Fe(II), (blue line) LS Fe(II).

Spin-transition properties. The magnetic property measurements of **[1Cl]** (Fig. 2(a)) show that the $\chi_m T$ value at room temperature is around. 3.2 cm^3 K mol^{-1}, where χ_m and T are the magnetic susceptibility and the temperature, respectively. Upon cooling, the $\chi_m T$ value decreases with decreasing temperature, approaching 0 cm^3 K mol^{-1} at 180 K. This result suggests that **[1Cl]** exhibits a gradual spin transition at $T_{1/2} \approx 268$ K ($T_{1/2}$ is the temperature at which HS and LS fractions are equal to each other).

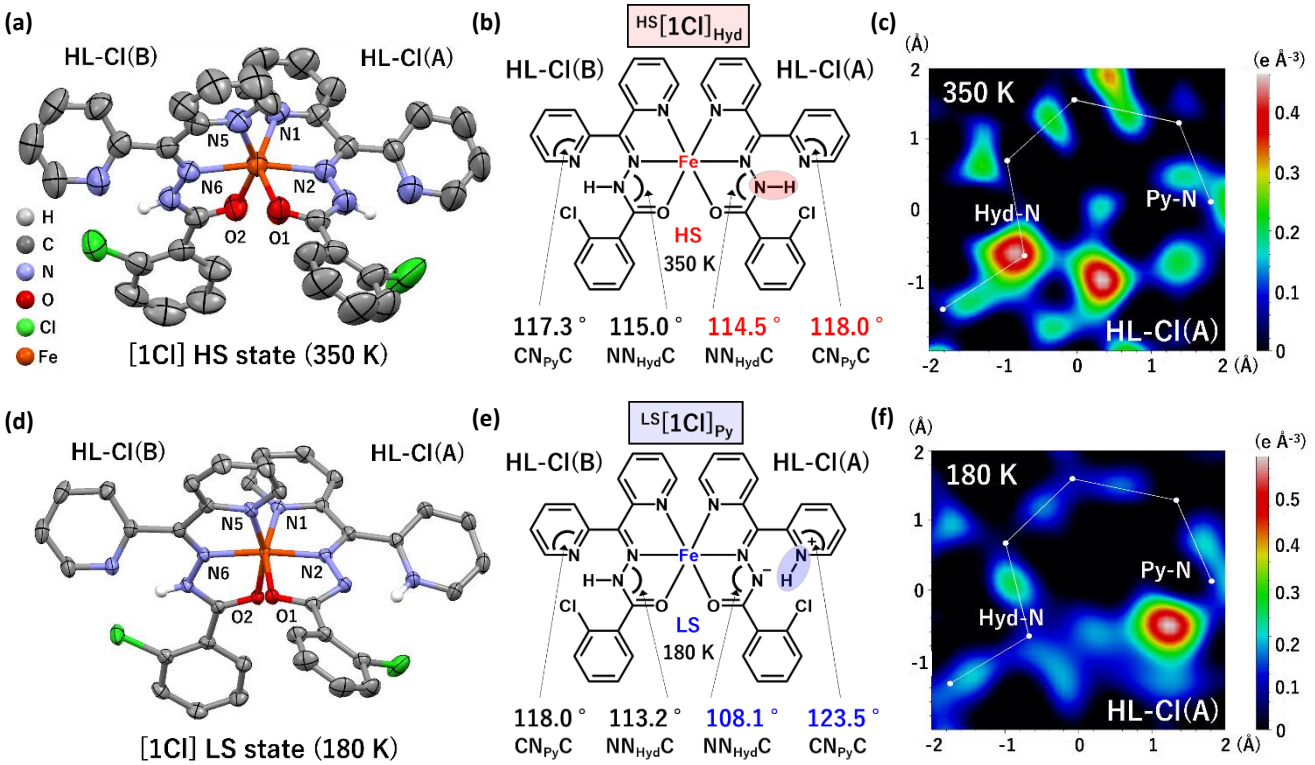

Figure 3. (a) Single-crystal molecular structure of **[1Cl]** at 350 K, showing 50% probability-of-displacement ellipsoids. The AsF_6^- anion and the hydrogen atoms that coordinate with carbon are omitted for clarity. (b) Schematic of the molecular structure, coordination angles, and spin state of **[1Cl]** at 350 K. (c) Difference Fourier map around the intramolecular hydrogen bond in HL-Cl(A) at 350 K; the H atom is located on the Hyd-N. The electron density at the maximum part in HL-Cl(A) and the standard deviation were 0.41 and 0.077 e $Å^{-3}$, respectively. (d) Molecular structure of **[1Cl]** at 180 K. (e) Schematic of the molecular structure, coordination angles, and spin state of **[1Cl]** at 180 K. (f) Difference Fourier map around the intramolecular hydrogen bond in HL-Cl(A) at 180 K; the H atom is located on Py-N. The electron density of the maximum part about HL-Cl(A) and the standard deviation were 0.59 and 0.08 e $Å^{-3}$, respectively.

The Mössbauer spectrum of **[1Cl]** (Fig. 2(b) and Table S1) at 300 K shows quadrupole doublet peaks originating from both the Fe(II) HS isomer (isomer shift (IS) = 0.792(7) mm s^{-1}, quadrupole splitting (QS) = 2.544(14) mm s^{-1}) and Fe(II) LS isomer (IS = 0.10(7), QS = 0.99(15)). The estimated fractions of Fe(II) HS and LS isomers at 300 K were 86% and 14%, respectively. The spectrum at 60 K shows a single quadrupole doublet originating from the Fe(II) LS isomer (IS = 0.292(8), QS = 0.913(14) mm s^{-1}). These results are consistent with the occurrence of a spin transition.

The temperature-dependent crystal structures of **[1Cl]** were measured; all of the crystallographic information and crystal structural parameters are listed in the Supporting Information (Tables S2 and S3). Variable-temperature single-crystal X-ray diffraction measurements were carried out at 180 and 350 K to investigate structural changes that occur with temperature variation (Fig. 3(a)–3(f)). The molecular packing and the labeling scheme are summarized in the Supporting Information (Fig. S1). The metal-to-ligand bond lengths between the Fe(II) and the azomethine-N at 350 K are 2.111(6) and 2.122(5) Å, which are characteristic of an HS Fe(II) complex. By contrast, the bond lengths at 180 K are 1.851(2) and 1.870(2) Å, which indicates that the Fe(II) is in the LS state. These results also indicate the occurrence of a spin transition.

Proton-transfer properties. Single-crystal analysis reveals that, in the asymmetric unit of **[1Cl]** (Fig. 3(a)), two crystallographically independent ligands coordinate to the Fe(II) cation, which implies that two kinds of intramolecular hydrogen bonds are formed between Hyd-N and Py-N in **[1Cl]**. One of these ligands forms a shorter N···N distance (Py-N···Hyd-N = 2.630(9) Å at 350 K) and is hereafter designated as HL-Cl(A). The other ligand forms a longer N···N distance (Py-N···Hyd-N = 2.693(8) Å at 350 K) and is designated as HL-Cl(B). The positions of the protons in HL-Cl(A) and HL-Cl(B) can be determined from the $CN_{Py}C$ angle and the $NN_{Hyd}C$ angle. Upon protonation of Py-N and Hyd-N, their bond angles tend to increase. The $CN_{Py}C$ angle has been reported to change from approximately 117° to 123° upon protonation on Py-N [28]. Furthermore, we listed the $NN_{Hyd}C$ angles reported for the crystal structures of hydrazone complexes (Table S4), which show that the $NN_{Hyd}C$ angles increased from approximately 109° to 114° upon protonation on Hyd-N.

At 350 K (Fig. 3(a)), the $NN_{Hyd}C$ angles in HL-Cl(A) and HL-Cl(B) are 114.5(5)° and 115.0(5)°, respectively, which are characteristic of protonated Hyd-N atoms (Fig. 3(b)). The $CN_{Py}C$ angles in HL-Cl(A) and HL-Cl(B) are 118.0(7)°and 117.3(6)°, respectively, which are characteristic of non-protonated Py-N atoms. Therefore, the protons in both HL-Cl(A) and HL-Cl(B) were located on Hyd-N at 350 K. The maximum electron density in the difference Fourier maps around the Hyd-N and Py-N in the HL-Cl(A) and HL-Cl(B) ligands at 350 and 180 K presented the information of the shift of the hydrogen atom position with temperature change. At 350 K, the maximum electron density attributable to H atoms located on Hyd-

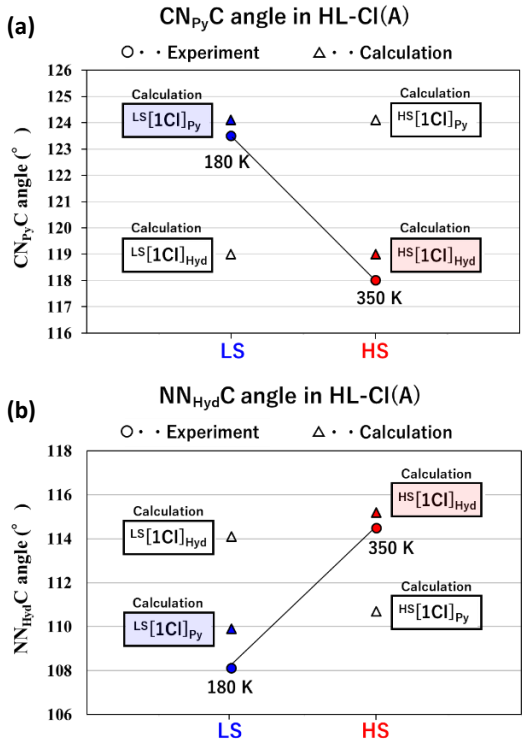

Figure 4. (a) $CN_{Py}C$ angles in HL-Cl(A); experimental results (o) at 180 K (LS state) and 350 K (HS state) and DFT calculation results (Δ) for ^{HS}**[1Cl]**$_{Hyd}$, ^{LS}**[1Cl]**$_{Hyd}$, ^{HS}**[1Cl]**$_{Py}$, and ^{LS}**[1Cl]**$_{Py}$. (b) $NN_{Hyd}C$ angles in HL-Cl(A); experimental results at 180 K (LS state) and 350 K (HS stae) and DFT calculation results for ^{HS}**[1Cl]**$_{Hyd}$, ^{LS}**[1Cl]**$_{Hyd}$, ^{HS}**[1Cl]**$_{Py}$, and ^{LS}**[1Cl]**$_{Py}$.

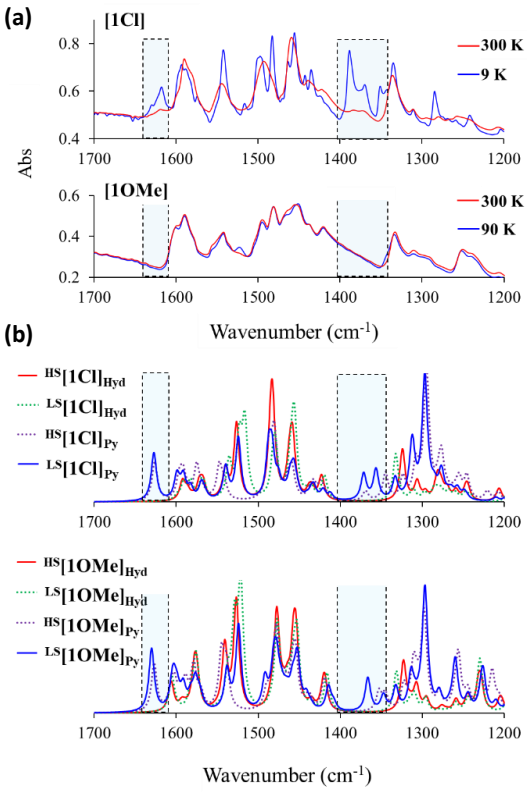

Figure 5. (a) Temperature dependence of the IR spectra of **[1Cl]** (top) and **[1OMe]** (bottom). Because the baselines slightly shifted during the temperature change, offsets have been added to the spectra of **[1Cl]** and **[1OMe]** so that the absorbances at 1700 cm^{-1} are the same. (b) The IR spectra calculated by DFT with a scaling factor of 0.98: **[1Cl]** (top) and **[1OMe]** (bottom).

N in both HL-Cl(A) and HL-Cl(B), suggesting that Hyd-N hosts the H atom in both ligands (Figs. 3(c) and S1). At 180 K (Fig. 3(d)), the $NN_{Hyd}C$ and the $CN_{Py}C$ angles in HL-Cl(B) are 113.2(2)° and 118.0(2)°, respectively. These values indicate that the proton in HL-Cl(B) remains on Hyd-N after the sample is cooled from 350 to 180 K (Fig. 3(e)). In HL-Cl(A), the $NN_{Hyd}C$ and the $CN_{Py}C$ angles are 108.1(2)° and 123.5(2)°, respectively. The change in these angles demonstrates that the proton was transferred from Hyd-N to Py-N upon cooling from 350 to 180 K (Fig. 3(b) and 3(e)). The difference Fourier map around Hyd-N and Py-N in HL-Cl(A) at 180 K shows that the H atom in HL-Cl(A) is located on Py-N (Fig. 3(f)), whereas that around Hyd-N and Py-N in HL-Cl(B) at 180 K shows that the H atom in HL-Cl(B) is located on Hyd-N (Fig. S1). Therefore, proton transfer occurred in only one of the two HL ligands. This result is consistent with the general tendency of polyprotic acids, in which the second deprotonation is less favorable than the first one.

Proton-transfer-coupled spin transition (PCST). The aforementioned experimental results reveal that PCST occurs in **[1Cl]**, where proton transfer occurs in only one of the two ligands, i.e., HL-Cl(A). The PCST process is expressed as

$$^{LS}\textbf{[1Cl]}_{Py} \rightleftarrows {}^{HS}\textbf{[1Cl]}_{Hyd}$$

To confirm the PCST, we carried out density-functional theory (DFT) calculations to estimate the values of the $CN_{Py}C$ and $NN_{Hyd}C$ angles (Table S5) in ^{HS}**[1Cl]**$_{Hyd}$, ^{HS}**[1Cl]**$_{Py}$, ^{LS}**[1Cl]**$_{Hyd}$, and ^{LS}**[1Cl]**$_{Py}$ (Fig. 1(b)). The calculated $CN_{Py}C$ and $NN_{Hyd}C$ angles of HL-Cl(A) are shown in Fig. 4(a) and 4(b), respectively. Figure. 4(a) reveals that the experimental $CN_{Py}C$ angle (123.5°) of the LS state at 180 K is consistent with the calculated value of 124.1° for ^{LS}**[1Cl]**$_{Py}$ but differs substantially from the value of 119.0° for ^{LS}**[1Cl]**$_{Hyd}$. The experimental $CN_{Py}C$ angle (118.0°) of the HS state at 350 K is consistent with the calculated value (118.8°) of ^{HS}**[1Cl]**$_{Hyd}$ but not with that (124.1°) of ^{HS}**[1Cl]**$_{Py}$. The comparison of DFT and experimental results supports the occurrence of PCST. Fig. 4(b) reveals that experimental $NN_{Hyd}C$ angle (108.1°) of LS state at 180 K is consistent with calculation value (109.9°) for ^{LS}**[1Cl]**$_{Py}$ but differs from that (114.2°) of ^{LS}**[1Cl]**$_{Hyd}$. The experimental $NN_{Hyd}C$ angle (114.5°) of the HS state at 350 K is consistent with calculation value (115.2°) for ^{HS}**[1Cl]**$_{Hyd}$ but not with that (110.7°) of ^{HS}**[1Cl]**$_{Py}$. These results also support the occurrence of PCST.

IR spectra of PCST process. Variable-temperature IR spectra of **[1Cl]** in the fingerprint region between 1200 and 1700 cm^{-1} were recorded to characterize the PCST behavior (Fig. 5(a)). The IR spectra show a clear change at the spin-transition temperature. One characteristic change observed is the appearance of peaks at around 1389 and 1370 cm^{-1} upon cooling, at approximately the temperature of the spin transition. To gain insight into the spectra, we performed DFT calculations for ^{HS}**[1Cl]**$_{Hyd}$, ^{HS}**[1Cl]**$_{Py}$, ^{LS}**[1Cl]**$_{Hyd}$, and ^{LS}**[1Cl]**$_{Py}$ (Fig. 5(b)). The simulated spectra indicate that the two peaks at 1371 and 1356 cm^{-1} appear upon PCST from the HS to the LS state; however, they do not appear upon the spin transition occurring without proton transfer. The peaks at 1371 and 1356 cm^{-1}, which correspond to the experimentally observed peaks centered at 1389 and 1370 cm^{-1}, respectively, originate mainly from the in-

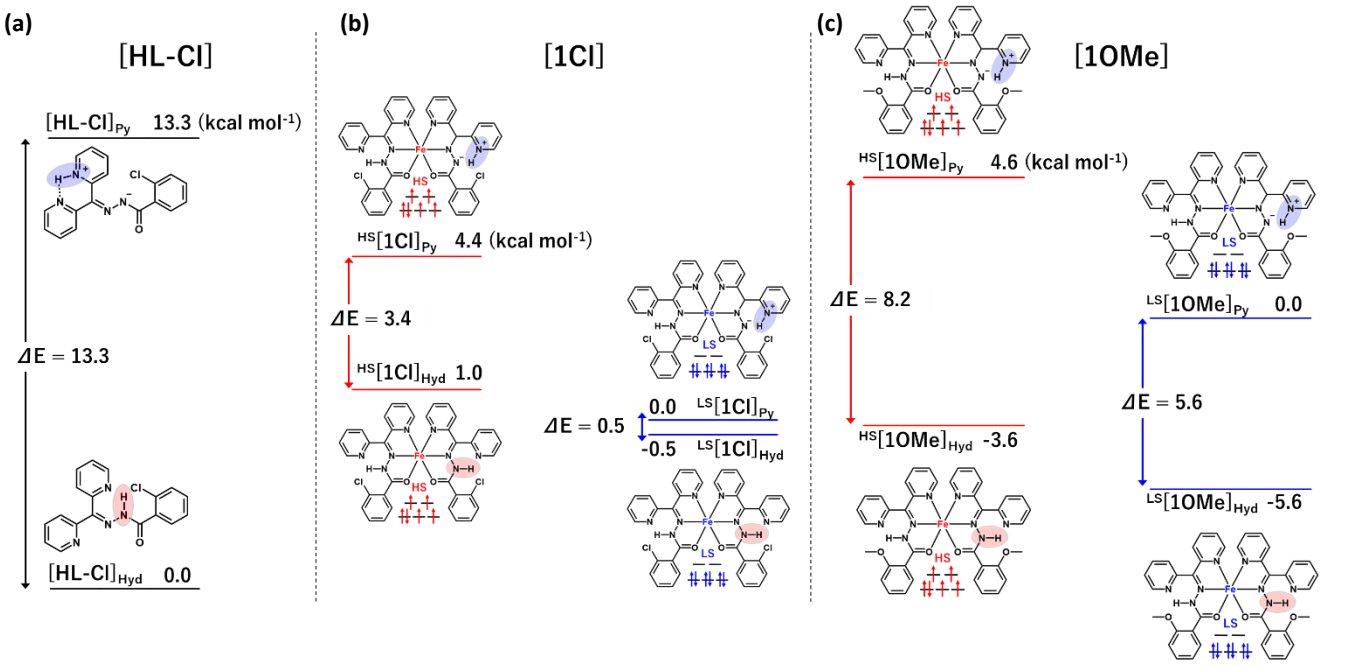

Figure 6. Calculated energy diagrams of (a) **[HL-Cl]**, (b) **[1Cl]** and (c) **[1OMe]**. The energies of **[HL-Cl]**, **[1Cl]** and **[1OMe]** are relative to $\mathbf{[HL\text{-}Cl]_{Hyd}}$, $^{LS}\mathbf{[1Cl]_{Py}}$ and $^{LS}\mathbf{[1OMe]_{Py}}$, respectively. The units are in kcal mol^{-1}. For $\mathbf{[HL\text{-}Cl]_{Py}}$, the structure with the [(Py-N)–H···(Py-N)] hydrogen bond was obtained for optimization calculations. Any structures having [(Py-N)–H···(Hyd-N)] hydrogen bond could not be optimized as a local minimum; the proton was always located on Hyd-N in **[HL-Cl]**.

plane N–H and C–H bending vibrations in the protonated pyridine ring coupled with the C–N stretching and C–N bending vibrations in the deprotonated hydrazone moiety [29-30]. The appearance of these peaks indicates that the proton at Hyd-N in HL-Cl(A) transferred to Py-N with decreasing temperature. Thus, the spin transition is accompanied by proton transfer. Additionally, DFT calculations reveal that another characteristic peak assigned to in-plane Py-N–H bending vibration should appear at 1626 cm^{-1} after the proton-coupled spin transition from the HS to the LS state for **[1Cl]** is completed. The IR spectra depict the corresponding in-plane Py-N–H bending vibration as a sharp peak at 1616 cm^{-1} for **[1Cl]**. These results are consistent with the occurrence of PCST in **[1Cl]**.

To further confirm the PCST behavior, the variable-temperature IR spectrum of the reference complex, **[1OMe]**, was recorded. Magnetization and Mössbauer measurements reveal that **[1OMe]** exhibits one-step spin transitions (Fig. S3 and Table S1). The changes in the $CN_{Py}C$ and $NN_{Hyd}C$ bond angles (Fig. S4 and Table S3) show that **[1OMe]** exhibits a spin transition without proton transfer.

$$^{LS}\mathbf{[1OMe]_{Hyd}} \rightleftarrows {}^{HS}\mathbf{[1OMe]_{Hyd}}$$

Figure 5 shows that the IR spectrum of **[1OMe]** differs from **[1Cl]**. Characteristic changes observed in the spectrum of **[1Cl]** at around 1389, 1370 and 1616 cm^{-1}, do not appear in the spectrum of **[1OMe]**. The experimental IR results for **[1OMe]** (Fig. 5(a)) is consistent with the IR spectra obtained using DFT calculations (Fig. 5(b)). These results support the occurrence of PCST in **[1Cl]** and the occurrence of only a spin transition without proton transfer in **[1OMe]**.

Mechanism of PCST: DFT calculation. To elucidate the PCST behavior, we calculated energies of **[1Cl]** by DFT method (Fig. 6). The DFT results show that the energies of $^{HS}\mathbf{[1Cl]_{Py}}$, $^{HS}\mathbf{[1Cl]_{Hyd}}$, $^{LS}\mathbf{[1Cl]_{Py}}$, and $^{LS}\mathbf{[1Cl]_{Hyd}}$ are 4.4, 1.0, 0.0, and −0.5 kcal mol^{-1}, respectively (Fig. 6(b)). Regarding the HS state, $^{HS}\mathbf{[1Cl]_{Hyd}}$ is more energetically stable than $^{HS}\mathbf{[1Cl]_{Py}}$, which is consistent with the experimental result, i.e., a proton is on Hyd-N at the HS state. By contrast, the energies of the LS state show that $^{LS}\mathbf{[1Cl]_{Hyd}}$ is also more stable than $^{LS}\mathbf{[1Cl]_{Py}}$, which is inconsistent with the experimental observations. However, the energy difference is only 0.5 kcal mol^{-1}. Given that the calculations are performed for isolated molecules without taking intermolecular interactions into account, the DFT results qualitatively reflect the experimental results in the sense that the energy of $^{LS}\mathbf{[1Cl]_{Py}}$ is greatly stabilized against $^{LS}\mathbf{[1Cl]_{Hyd}}$ (the energy difference is merely 0.5 kcal mol^{-1}) compared with the HS state (the difference is 3.4 kcal mol^{-1}).

To gain further insight into the PCST behavior, the energies of the HL-Cl ligand that does not coordinate to Fe(II) were also calculated (Fig. 6(a)). The energy of one of the optimized forms of HL-Cl, wherein the proton is located on Hyd-N (hereafter denoted as $\mathbf{[HL\text{-}Cl]_{Hyd}}$), is 0 kcal mol^{-1}, whereas the energy of the other form, wherein the proton is located on Py-N (hereafter denoted as $\mathbf{[HL\text{-}Cl]_{Py}}$) is 13.3 kcal mol^{-1}. Now, we compare the energy difference of each state. First, we compare the energies of $\mathbf{[HL\text{-}Cl]_{Py}}$ and $\mathbf{[HL\text{-}Cl]_{Hyd}}$. The $\mathbf{[HL\text{-}Cl]_{Hyd}}$ state is more stable than the $\mathbf{[HL\text{-}Cl]_{Py}}$ state by 13.3 kcal mol^{-1} (Fig. 6(a)), meaning that proton is located on Hyd-N. This result is consistent with the reported p*K*a values of Hyd-N and Py-N in the keto tautomer of hydrazone-type ligands being in the ranges 9.17–13.76 and 2.34–4.15, respectively [30-32]. Next, we consider the case where the HL-Cl ligand coordinates to HS Fe(II). When HL-Cl coordinates to HS Fe(II), an electron pair of HL-Cl is donated to Fe(II). The coordination strongly influences the property of Hyd-N rather than Py-N in the remote site; the complexation has been reported to lead to a great increase in the acidity of Hyd-N [33]. Indeed, the energy difference (3.4 kcal mol^{-1}) between $^{HS}\mathbf{[1Cl]_{Py}}$ and $^{HS}\mathbf{[1Cl]_{Hyd}}$ (Fig. 6(b), left) became much smaller than that (13.3 kcal mol^{-1}) between $\mathbf{[HL\text{-}Cl]_{Py}}$ and $\mathbf{[HL\text{-}Cl]_{Hyd}}$ (Fig. 6(a)) even though Hyd-N is

still the stable position for the proton. Finally, we consider the process by which the HS Fe(II) changes to LS Fe(II). The energy difference (0.5 kcal mol^{-1}) between ^{LS}**[1Cl]**$_{Py}$ and ^{LS}**[1Cl]**$_{Hyd}$ (Fig. 6(b), right) decreases compared with that (3.4 kcal mol^{-1}) between ^{HS}**[1Cl]**$_{Py}$ and ^{HS}**[1Cl]**$_{Hyd}$ (Fig. 6(b), left). This result suggests that, upon spin transition from HS to LS, the electron is slightly more donated from the HL-Cl ligand to the Fe(II) center, thereby destabilizing the Hyd-N site and making Py-N a more favorable site. The atomic polar tensor (APT) charge on Fe(II) shows that the electron on the ligand partially shifts to Fe(II) upon transition from HS to LS. The differences in the APT charge on Fe induced by spin transition from ^{HS}**[1Cl]**$_{Hyd}$ to ^{LS}**[1Cl]**$_{Hyd}$ and from ^{HS}**[1Cl]**$_{Py}$ to ^{LS}**[1Cl]**$_{Py}$ are −1.39 and −1.37, respectively. The changes in the APT charge are in agreement with the explanation that the slight charge redistribution from the ligand to Fe(II) occurs upon transition from HS to LS. The changes in the energy levels **[1OMe]** is similar to that calculated for **[1Cl]** (Fig. 6(c)). A distinct difference between **[1OMe]** and **[1Cl]** is that **[1OMe]**$_{Hyd}$ is much more stable than **[1OMe]**$_{Py}$ for both the HS and LS states. This is attributable to the electron-donating substituent OMe that reduces the acidity of Hyd-N. Thus, the proton should be located on Hyd-N independent on the spin state. This is consistent with the experimental result that spin transition in **[1OMe]** is not coupled with proton transfer. The trend in the change of the energy difference shown in Fig. 6 is qualitatively consistent with the experimental results.

Photoinduced proton transfer. The aforementioned experimental results and the DFT calculations clearly show that proton transfer and spin transition were coupled in **[1Cl]**, which is the first crystalline compound to demonstrate PCST. The synthesis of correlation systems is important in that they can exhibit superior functions through synergy of the coupled components. Spin-transition behavior is known to be induced by light. Furthermore, Fe(II) spin-transition complexes that contain hydrazone-type ligands have been reported to exhibit LIESST under irradiation with 532-nm-wavelength light [19-22]. Therefore, the successful preparation of the PCST Fe(II) compounds potentially enables the observation of the induction of PCST by light and the trapping of the resultant excited state at low temperatures. Thus, in terms of proton manipulation, proton transfer by light and the trapping of the excited proton transfer state can be realized via the PCST mechanism. We therefore examined the photoeffects of **[1Cl]**.

Time-resolved IR absorption measurements were performed at 190 K using femtosecond laser pulses (Fig. 7). Figure 7(b) shows that several transient absorption bands are observed at 2.5 ps after the excitation. The intensities of these transient absorption bands increase with increasing delay time within 50 ps (Fig. 7(c)). However, the intensities and the spectral patterns do not change after the delay time of 50 ps (Figs. 7(c) and S2). The transient IR spectrum collected at 50 ps after the excitation is in good agreement with the IR difference spectrum between the ^{HS}**[1Cl]**$_{Hyd}$ state at 300 K and the ^{LS}**[1Cl]**$_{Py}$ state at 9 K (Fig. 7(a)). These results reveal that PCST is induced by light and is completed within *ca*. 50 ps. Notably, the spectral pattern of the transient IR spectrum at the delay time of 0 ps appears to differ slightly from the patterns of the spectra after 2.5 ps (Fig. 7(b)). Moreover, the changes in spectral patterns with isosbestic points were observed after the delay time of 0 ps. These observations indicate that the HS state is photogenerated via one other excited state.

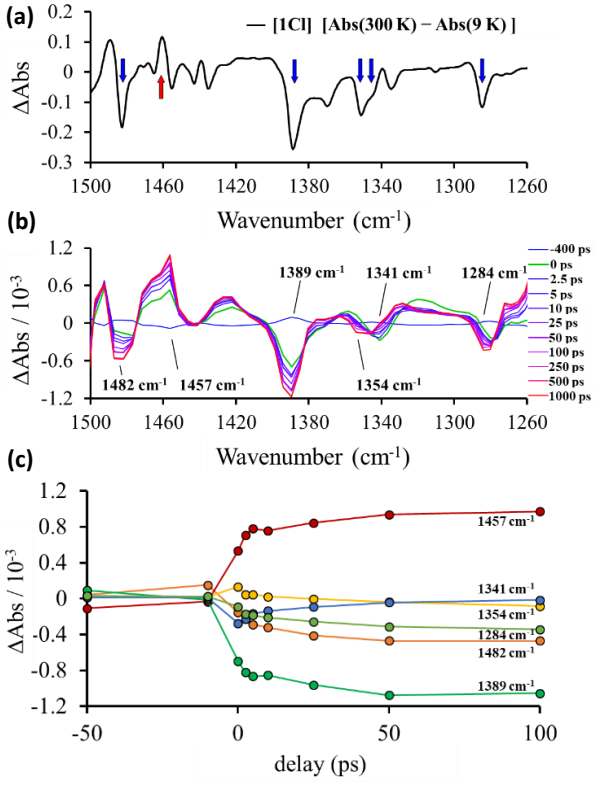

Figure 7. (a) IR difference spectrum of **[1Cl]** between ^{HS}**[1Cl]**$_{Hyd}$ at 300 K and ^{LS}**[1Cl]**$_{Py}$ at 9 K. (b) Time-resolved IR spectra of **[1Cl]** excited at 532 nm (*ca.* 100 fs, 3 μJ pulse^{-1}). (c) Plots of time-resolved IR absorption intensities of **[1Cl]** against the delay time between the pump and probe pulses.

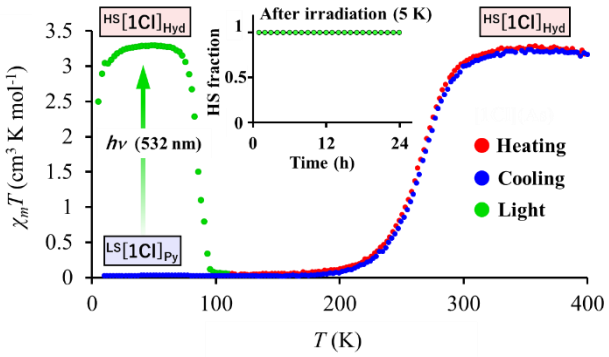

Figure 8. $\chi_m T$–T plots for **[1Cl]** before and after irradiation with 532-nm light. The inset shows the change in HS fraction with time after irradiation at 5 K; the light-induced excited state is substantially trapped. The HS fraction value is normalized as 1 at $t = 0$.

Trapping of photoinduced metastable proton-transfer state. We also investigated the photoeffect at low temperature to explore the trapping of the metastable state. First, we characterized the photoeffect using a SQUID magnetometer. A photoinduced increase in the $\chi_m T$ value was observed upon irradiating ^{LS}**[1Cl]**$_{Py}$ at 5 K with 532, 660, and 780 nm light, which corresponds to excitation of the edge or center of the metal-to-ligand charge-transfer band (Fig. S2) [29-30, 32, 34]. Figure 8 shows the $\chi_m T$–T plot before and after irradiation with 532 nm light at 5 K. The increase in the $\chi_m T$ value after excitation indicates that the spin transition from LS to HS is induced and that the resultant excited HS state is trapped as a metastable state (LIESST effect). The change in magnetization with time shows that the

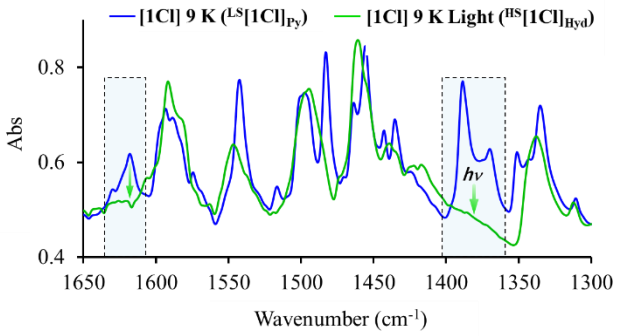

Figure 9. The IR spectra of **[1Cl]** before and after irradiation with a 532-nm light at 9 K.

decrease in the magnetization value is less than several percent even 24 h after irradiation, demonstrating that the light-induced excited state is substantially trapped (Fig. 8). When the magnetic moment is measured after irradiation during the heating mode from 5 K to above 100 K, the $\chi_m T$ value abruptly decreases at around 85 K, meaning that the trapped HS state relaxed back to the LS state.

IR spectroscopy was used to further examine the trapped state after irradiation. As previously described, characteristic peaks centered at 1389 and 1370 cm^{-1} and a sharp peak at 1616 cm^{-1} were observed in the IR spectrum of **[1Cl]** at 9 K before irradiation. After light irradiation, the intensities of the peaks centered at 1389, 1370 and 1616 cm^{-1} decreased and the overall IR spectrum became similar to that corresponding to the high-temperature phase (Fig. 9). The IR difference spectrum of **[1Cl]** between before and after irradiation corresponds with that between the HS state (300 K) and the LS state (9 K) (Fig. S2). These results reveal that the trapped state after irradiation is expressed as ^{HS}**[1Cl]**$_{Hyd}$. Thus, PCST is induced by light, and the resultant excited state is trapped as a metastable state, which is expressed as

$$^{LS}\mathbf{[1Cl]}_{Py} \rightarrow {}^{HS}\mathbf{[1Cl]}_{Hyd} \text{ (excited state)}.$$

In terms of proton position, **[1Cl]** undergoes light-induced proton transfer from Py-N to Hyd-N and the metastable proton-transfer state, wherein the proton lies on Hyd-N, is trapped at low temperatures.

The trapping of the metastable state after irradiation is also confirmed by the single-crystal structure. Figure 8 shows that **[1Cl]** exhibited LIESST with a high conversion ratio of nearly 1, which is in contrast to typical photofunctional molecules; normally, limited moieties exhibit photoisomerization in crystalline states because of steric hindrance [35-38]. Furthermore, the photoinduced change occurs as a single-crystal-to-single-crystal transition. Thus, structures of the photoinduced state are precisely determined by X-ray single-crystal analysis [39-40]. The crystal structure after irradiation shows only one independent Fe(II) complex, and the coordination distances around Fe(II) were characteristic of an HS complex (Fig. 10(a) and Table S3). Single-crystal analysis shows that, under irradiation of **[1Cl]**, the $NN_{Hyd}C$ and $CN_{Py}C$ angles in HL-Cl(A) changed from 108.1° to 114.2° and from 123.4° to 118.4°, respectively (Fig. 10(b)); these values reveal that the protons in HL-Cl(A) transferred from Py-N to Hyd-N in conjunction with the occurrence of the light-induced spin transition. These results demonstrate

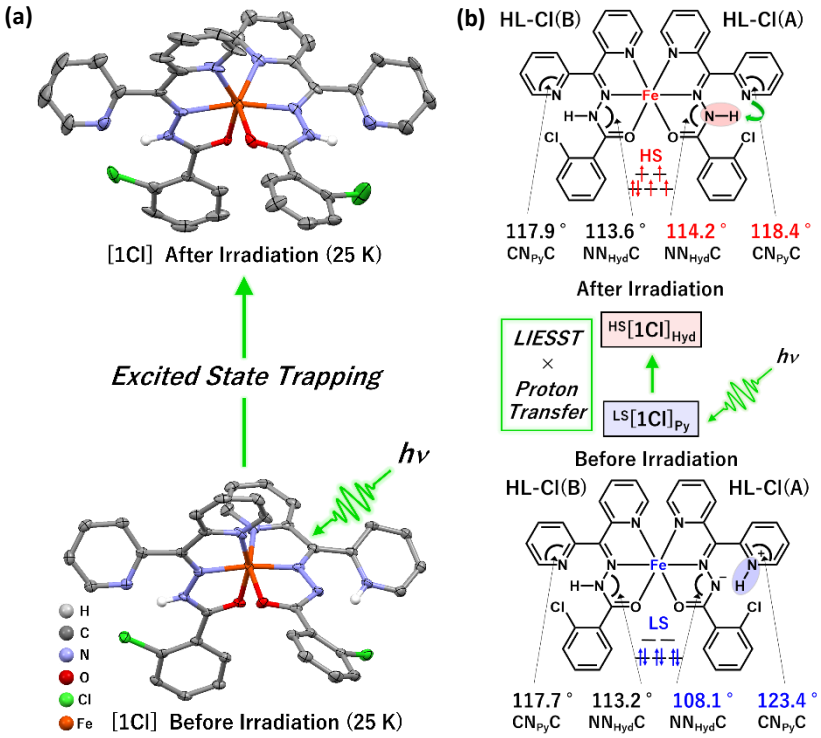

Figure 10. Crystal structural changes with PCST. (a) Crystal structure of **[1Cl]** before (bottom) and after (top) irradiation with 532-nm light at 25 K. The AsF_6^- anions and the hydrogen atoms coordinating with carbon atoms are omitted for clarity. (b) Schematic of the molecular structure, coordination angles, and spin state of **[1Cl]** before (bottom) and after (top) irradiation with 532-nm light at 25 K. The values of $NN_{Hyd}C$ and $CN_{Py}C$ angles demonstrate the photoinduced proton transfer from Py-N to Hyd-N in conjunction with the spin transition from LS to HS under irradiation with 532-nm light.

that **[1Cl]** undergoes light-induced PCST, wherein the proton position can be switched between two sites (Fig. 10(b)).

CONCLUSIONS

To realize synergistic properties derived from the proton–electron coupling mechanism, we attempted to synthesize an Fe(II) complex that exhibits PCST. Through precise molecular design, we succeeded in synthesizing an Fe(II) complex, **[1Cl]** that exhibits PCST. This work represents the first demonstration of the thermally induced PCST phenomenon in a crystalline material. Furthermore, **[1Cl]** exhibits photoinduced PCST and trapping of the photoinduced metastable state through coupling of proton transfer and the light-induced spin transition effect and coupling of proton transfer and the LIESST effect, respectively. Furthermore, when the PCST phenomenon is viewed in terms of proton manipulation, photocontrol of proton transfer and the trapping of the photoinduced metastable proton-transfer state are realized through synergistic effects. The bistability of the light-controllable proton position is useful for switching proton-based functionalities between two properties in molecular devices. Notably, the correlation systems with the PCST mechanism have the potential to exhibit various other proton- and spin-based functionalities through cross-correlation effects. Furthermore, we believe our study will be useful in the development of the interdisciplinary field of molecular protonics, electronics, and photonics.

EXPERIMENTAL SECTION

Magnetic property measurement. Magnetic susceptibility measurements for **[1Cl]** and **[1OMe]** were conducted on a Quantum Design MPMS-5S superconducting quantum-interference device magnetometer under a 5-kOe field, with a sweeping rate of 3 K min^{-1}. The measurement samples were prepared by encapsulating each crystalline compound into a gelatin capsule except for the photomagnetic measurements. Compound magnetic susceptibility measurements, in the light-excited state, were performed after sample irradiation with 532 nm green light for 1.5 h. The samples subjected to irradiation were prepared by spreading powdered samples onto colorless tape.

Mössbauer spectroscopy. ^{57}Fe Mössbauer spectra were recorded on a constant acceleration spectrometer with a source of ^{57}Co/Rh in the transmission mode. The measurements were performed using a closed-cycle helium refrigerator (Iwatani Co., Ltd or ULVAC CRYOGENICS INC) and a conventional Mössbauer spectrometer (Wissel MVT-1000 or Topologic Systems). All isomer shifts are given relative to α-Fe at room temperature. The Mössbauer spectra were fitted with the least-squares fitting program MossWinn 4.0.

IR spectroscopy. The IR spectra of **[1Cl]** at 300 and 9 K and **[1Cl]** at 9 K before and after light (532 nm) irradiation were recorded using an FT-IR spectrophotometer (VERTEX 70, Bruker) equipped with a closed-cycle helium refrigerator cryostat (Nagase Techno-Engineering). The ground-powdered samples were held between a grained and a plane CaF_2 plates. A solid-state cw green laser (Millennia, Spectra Physics) was used as the illumination light source. The laser wavelength was 532 nm, and the power density was 15 mW cm^{-2} at the sample point. Temperature-dependent IR spectra of **[1OMe]** were recorded using an FT-IR spectrophotometer (FT/IR-660 plus, Jasco) equipped with a helium-flow-type refrigerator (Helitran LT-3–110). Samples were prepared by depositing ground-powdered samples onto the CaF_2 plates.

The experimental setup of picosecond time-resolved IR absorption measurements is described as follows. The fundamental output from a Ti:sapphire regenerative amplifier (Solstice Ace, Spectra Physics; wavelength 800 nm, power 5 W, repetition rate 1 kHz, pulse width ~100 fs) was divided into two beams. Both were used to excite two optical parametric amplifiers (OPAs) and generate pump and probe pulses. The probe IR pulse was obtained by difference-frequency generation between the signal and idler waves from one OPA (TOPAS-C, Light Conversion). The center wavelength of the IR pulse was 7200 nm, and its spectral bandwidth was ~170 cm^{-1} in FWHM. The probe beam was divided into two paths by a ZnSe half mirror. One portion of the beam was focused on and transmitted through the sample; it was used as a sample beam. The other was used as a reference beam. Both were introduced into a 19 cm spectrograph (TRIAX190, HORIBA JOBIN YVON) with a slightly different height offset. The dispersed two beams were simultaneously detected by a 2 × 64-channel liquid-nitrogen-cooled HgCdTe detector array and integrated by 128 box-car integrators (IR-12-128, InfraRed Associates). The normalized IR signals were obtained by dividing the sample intensities by the reference intensities. The pump green pulse (532 nm) was obtained by sum-frequency generation of the idler wave and the excitation pulse (800 nm) from the other OPA (TOPAS-prime, Light Conversion). The pump beam was modulated at half the repetition rate of the probe beam (500 Hz) by a mechanical chopper. The modulated pump beam was passed through a delay stage and focused on the sample noncollinearly relative to the probe beam. The normalized IR signals with and without the pump pulses were separately accumulated by a computer. The pump-induced infrared absorption was obtained by dividing the pump-on signal by the pump-off signal. The cross-correlation time between the pump and probe pulses, which was determined by the rise of a transient infrared absorption of photoexcited silicon due to free carriers, was ~0.5 ps. The energy of the probe pulse at the sample position was less than 0.5 μJ, and that of the pump pulse was less than 1 μJ. **[1Cl]** was held between a grained and a plane CaF_2 plates. The sample was placed in a liquid nitrogen-cooled cryostat (OptistatDN-V, Oxford), and kept at 190 K, at which most of the sample was in the LS state. The total exposure time for each time delay was 20 min.

DFT calculation. All energy calculations for the $\mathbf{[1X]_{Hyd}}$ and $\mathbf{[1X]_{Py}}$ (X = Cl and OMe) complexes in the singlet and quintet spin states, and free ligands $\mathbf{[HL\text{-}Cl]_{Hyd}}$ and $\mathbf{[HL\text{-}Cl]_{Py}}$ were carried out using restricted and unrestricted B3LYP* functionals combined with the 6-311+G** basis set implemented in the Gaussian 09 package [41]. The B3LYP* functional, developed by Reiher and co-workers [42,43], is a reparametrized version of the B3LYP functional with 15% Hartree–Fock exchange instead of 20% in the original B3LYP functional[44-46]. The B3LYP* functional was specifically developed to provide the best performance for accurate spin-state splitting while the original B3LYP functional results in the overestimation of HS stability. For comparison with the experimental results, the calculated vibrational frequencies were rescaled by the factor of 0.98.

ASSOCIATED CONTENT

Supporting Information

The Supporting Information is available free of charge on the ACS Publications website at DOI:

Experimental conditions of synthesis, X-ray structural determination and UV-vis spectra measurement, structural parameters of the crystal structure and DFT calculations of all compounds, UV-vis spectra and time-resolved IR spectra of **[1Cl]**, and the crystal structure, magnetic property, and Mössbauer spectra of **[1OMe]**. X-ray crystallographic data for **[1Cl]** at 350, 180, and 25 K before and after irradiation of 532 nm light and for **[1OMe]** at 150 and 300 K (CIF).

AUTHOR INFORMATION

Corresponding Author

* sato@cm.kyushu-u.ac.jp

ACKNOWLEDGMENT

We thank for the support by MEXT KAKENHI (Grant Numbers JP17H01197, JP16H00849, JP17K05761, JP24109014, JP15K13710, JP17H01200, JP17H03117, JP16K05421 and JP17H06928), by the MEXT Project of "Integrated Research Consortium on Chemical Sciences", "Elements Strategy Initiative to Form Core Research Center", JST-CREST "Innovative Catalysts" JPMJCR15P5, and by the Cooperative Research Program of "Network Joint Research Center for Materials and Devices". The synchrotron radiation experiments were performed at the BL02B1 of SPring-8 with the approval of the Japan Synchrotron Radiation Research Institute (JASRI) (Proposal No. 2017A1364, 2017B1285, 2018A1213 and 2018B1259). This work was partly supported by Nanotechnology Platform Program (Molecule and Material Synthesis) of MEXT, Japan. The computation was carried out using the computer facilities at Research Institute for Information Technology, Kyushu University.

REFERENCES

(1) Li, A.-L.; Gao, Q.; Xu, J.; Bu, X.-H., Proton-conductive metal-organic frameworks: Recent advances and perspectives. *Coord. Chem. Rev.* **2017,** *344*, 54-82.

(2) Hemmatian, Z.; Keene, S.; Josberger, E.; Miyake, T.; Arboleda, C.; Soto-Rodríguez, J.; Baneyx, F.; Rolandi, M., Electronic control of H^+ current in a bioprotonic device with Gramicidin A and Alamethicin. *Nat. Commu.* **2016,** *7*, 12981.

(3) Weinberg, D. R.; Gagliardi, C. J.; Hull, J. F.; Murphy, C. F.; Kent, C. A.; Westlake, B. C.; Paul, A.; Ess, D. H.; McCafferty, D. G.; Meyer, T. J., Proton-Coupled Electron Transfer. *Chem. Rev.* **2012,** *112*, 4016-4093.

(4) Tokura, Y.; Seki, S., Multiferroics with Spiral Spin Orders. *Adv. Mater.* **2010,** *22*, 1554-1565.

(5) Ishiwata, S.; Taguchi, Y.; Murakawa, H.; Onose, Y.; Tokura, Y., Low-Magnetic-Field Control of Electric Polarization Vector in a Helimagnet. *Science* **2008,** *319*, 1643-1646.

(6) Reece, S. Y.; Nocera, D. G., Proton-Coupled Electron Transfer in Biology: Results from Synergistic Studies in Natural and Model Systems. *Annu. Rev. Biochem.* **2009**, *78*, 673-699.

(7) Nakasuji, K.; Sugiura, K.; Kitagawa, T.; Toyoda, J.; Okamoto, H.; Okaniwa, K.; Mitani, T.; Yamamoto, H.; Murata, I., Exploration of new cooperative proton-electron transfer (PET) systems: first example of extended conjugated quinhydrones, 1,5-dihalo-2,6-naphthoquinhydrones. *J. Am. Chem. Soc.* **1991,** *113*, 1862-1864.

(8) Horiuchi, S.; Tokunaga, Y.; Giovannetti, G.; Picozzi, S.; Itoh, H.; Shimano, R.; Kumai, R.; Tokura, Y., Above-room-temperature ferroelectricity in a single-component molecular crystal. *Nature* **2010,** *463*, 789-92.

(9) Ueda, A.; Yamada, S.; Isono, T.; Kamo, H.; Nakao, A.; Kumai, R.; Nakao, H.; Murakami, Y.; Yamamoto, K.; Nishio, Y.; Mori, H., Hydrogen-bond-dynamics-based switching of conductivity and magnetism: a phase transition caused by deuterium and electron transfer in a hydrogen-bonded purely organic conductor crystal. *J. Am. Chem. Soc.* **2014,** *136*, 12184-92.

(10) Mitsumi, M.; Ezaki, K.; Komatsu, Y.; Toriumi, K.; Miyatou, T.; Mizuno, M.; Azuma, N.; Miyazaki, Y.; Nakano, M.; Kitagawa, Y.; Hanashima, T.; Kiyanagi, R.; Ohhara, T.; Nakasuji, K., Proton Order-Disorder Phenomena in a Hydrogen-Bonded Rhodium-η^5-Semiquinone Complex: A Possible Dielectric Response Mechanism. *Chem. Eur. J.* **2015,** *21*, 9682-96.

(11) Kassem, S.; Lee, A. T. L.; Leigh, D. A.; Markevicius, A.; Sola, J., Pick-up, transport and release of a molecular cargo using a small-molecule robotic arm. *Nat. Chem.* **2016,** *8*, 138-143.

(12) Li, K.; Li, Y.; Tao, J.; Liu, L.; Wang, L.; Hou, H.; Tong, A., Crystal Violet Lactone Salicylaldehyde Hydrazone Zn(II) Complex: a Reversible Photochromic Material both in Solution and in Solid Matrix. *Sci. Rep.* **2015,** *5*, 14467.

(13) Ray, D.; Foy, J. T.; Hughes, R. P.; Aprahamian, I., A switching cascade of hydrazone-based rotary switches through coordination-coupled proton relays. *Nat. Chem.* **2012,** *4*, 757.

(14) Su, X.; Aprahamian, I., Hydrazone-based switches, metallo-assemblies and sensors. *Chem. Soc. Rev.* **2014,** *43*, 1963-1981.

(15) Rosario-Amorin, D.; Dechambenoit, P.; Bentaleb, A.; Rouzières, M.; Mathonière, C.; Clérac, R., Multistability at Room Temperature in a Bent-Shaped Spin-Crossover Complex Decorated with Long Alkyl Chains. *J. Am. Chem. Soc.* **2018,** *140*, 98-101.

(16) Romero-Morcillo, T.; Seredyuk, M.; Muñoz, M. C.; Real, J. A., Meltable Spin Transition Molecular Materials with Tunable Tc and Hysteresis Loop Width. *Angew. Chem. Int. Ed.* **2015,** *54*, 14777-14781.

(17) Chen, X.-Q.; Cai, Y.-D.; Jiang, W.; Peng, G.; Fang, J.-K.; Liu, J.-L.; Tong, M.-L.; Bao, X., A Multi-Stimuli-Responsive Fe(II) SCO Complex Based on an Acylhydrazone Ligand. *Inorg. Chem.* **2019,** *58*, 999-1002.

(18) Yuan, J.; Wu, S.-Q.; Liu, M.-J.; Sato, O.; Kou, H.-Z., Rhodamine 6G-Labeled Pyridyl Aroylhydrazone Fe(II) Complex Exhibiting Synergetic Spin Crossover and Fluorescence. *J. Am. Chem. Soc.* **2018,** *140*, 9426-9433.

(19) Zhang, L.; Wang, J.-J.; Xu, G.-C.; Li, J.; Jia, D.-Z.; Gao, S., Tuning size and magnetic thermal hysteresis in a new near room temperature spin crossover compound. *Dalton Trans.* **2013,** *42*, 8205-8208.

(20) Zhang, L.; Xu, G.-C.; Wang, Z.-M.; Gao, S., Two Mononuclear Iron(II) Spin-Crossover Complexes with a N_4O_2 Coordination Sphere. *Eur. J. Inorg. Chem.* **2013,** *2013*, 1043-1048.

(21) Zhang, L.; Xu, G.-C.; Xu, H.-B.; Mereacre, V.; Wang, Z.-M.; Powell, A. K.; Gao, S., Synthesis, magnetic and photomagnetic study of new iron(II) spin-crossover complexes with N_4O_2 coordination sphere. *Dalton Trans.* **2010,** *39*, 4856-4868.

(22) Zhang, L.; Xu, G.-C.; Xu, H.-B.; Zhang, T.; Wang, Z.-M.; Yuan, M.; Gao, S., Abrupt spin transition around room temperature and light induced properties in Fe^{II} complexes with N_4O_2 coordination sphere. *Chem. Commun.* **2010,** *46*, 2554-2556.

(23) Nakanishi, T.; Sato, O., Synthesis, Structure, and Magnetic Properties of New Spin Crossover Fe(II) Complexes Forming Short Hydrogen Bonds with Substituted Dicarboxylic Acids. *Crystals* **2016,** *6*, 8.

(24) Kuriakose, D.; Aravindakshan, A. A.; Kurup, M. R. P., Synthesis, spectroscopic, crystal structures and photoluminescence studies of cadmium(II) complexes derived from di-2-pyridyl ketone benzoylhydrazone: Crystal structure of a rare eight coordinate cadmium(II) complex. *Polyhedron* **2017,** *127*, 84-96.

(25) Reena, T. A.; Seena, E. B.; Prathapachandra Kurup, M. R., Zinc(II) complexes derived from di-2-pyridyl ketone N^4-phenyl-3-semicarbazone: Crystal structures and spectral studies. *Polyhedron* **2008,** *27*, 3461-3466.

(26) Bakir, M.; Conry, R., Synthesis, spectroscopic and X-ray crystallographic properties of manganese compounds of keto- and enol-coordinated di-2-pyridyl ketone benzoyl hydrazone (dpkbh). Reactions of $Mn(CO)_5Br$ with dpkbh. *J. Coord. Chem.* **2016,** *69*, 1244-1257.

(27) Kyriakidis, C. E.; Christidis, P. C.; Rentzeperis, P. J.; Tossidis, I. A., Crystal structure and spectra of dichloro-o-bromobenzoyldi-(2-pyridyl)ketonohydrazono zinc(II). *Z. Kristallogr.* **1990,** *193*, 261-269.

(28) Krygowski, T. M.; Szatyłowicz, H.; Zachara, J. E., How H-bonding Modifies Molecular Structure and π-Electron Delocalization in the Ring of Pyridine/Pyridinium Derivatives Involved in H-Bond Complexation. *J. Org. Chem.* **2005,** *70*, 8859-8865.

(29) Bernhardt, P. V.; Wilson, G. J.; Sharpe, P. C.; Kalinowski, D. S.; Richardson, D. R., Tuning the antiproliferative activity of biologically active iron chelators: characterization of the coordination chemistry and biological efficacy of 2-acetylpyridine and 2-benzoylpyridine hydrazone ligands. *J. Biol. Inorg. Chem.* **2008,** *13*, 107-119.

(30) Bernhardt, P. V.; Chin, P.; Sharpe, P. C.; Richardson, D. R., Hydrazone chelators for the treatment of iron overload disorders: iron coordination chemistry and biological activity. *Dalton Trans.* **2007,** 3232-3244.

(31) Suarez Iha, M. E. V.; Pehkonen, S. O.; Hoffmann, M. R., Stability, Stoichiometry, and Structure of Fe(II) and Fe(III) Complexes with Di-2-pyridyl Ketone Benzoylhydrazone: Environmental Applications. *Environ. Sci. Technol.* **1994,** *28*, 2080-2086.

(32) Bernhardt, P. V.; Caldwell, L. M.; Chaston, T. B.; Chin, P.; Richardson, D. R., Cytotoxic iron chelators: characterization of the structure, solution chemistry and redox activity of ligands and iron complexes of the di-2-pyridyl ketone isonicotinoyl hydrazone (HPKIH) analogues. *J. Biol. Inorg. Chem.* **2003,** *8*, 866-880.

(33) Chang, M.; Horiki, H.; Nakajima, K.; Kobayashi, A.; Chang, H. C.; Kato, M., Acid-Base Behavior of Substituted Hydrazone Complexes Controlled by the Coordination Geometry. *Bull. Chem. Soc. Jpn.* **2010,** *83*, 905-910.

(34) Shongwe, M. S.; Al-Rahbi, S. H.; Al-Azani, M. A.; Al-Muharbi, A. A.; Al-Mjeni, F.; Matoga, D.; Gismelseed, A.; Al-Omari, I. A.; Yousif, A.; Adams, H.; Morris, M. J.; Mikuriya, M., Coordination versatility of tridentate pyridyl aroylhydrazones towards iron: tracking down the elusive aroylhydrazono-based ferric spin-crossover molecular materials. *Dalton Trans.* **2012,** *41*, 2500-2514.

(35) Harada, J.; Uekusa, H.; Ohashi, Y., X-ray analysis of structural changes in photochromic salicylideneaniline crystals. Solid-state reaction induced by two-photon excitation. *J. Am. Chem. Soc.* **1999,** *121*, 5809-5810.

(36) Koshima, H.; Takechi, K.; Uchimoto, H.; Shiro, M.; Hashizume, D., Photomechanical bending of salicylideneaniline crystals. *Chem. Commun.* **2011,** *47*, 11423-11425.

(37) Yamazaki, Y.; Sekine, A.; Uekusa, H., In Situ Control of Photochromic Behavior through Dual Photo-Isomerization Wing Cobaloxime Complexes with Salicylidene-3-aminopyridine and 3-Cyanopropyl Ligands. *Cryst. Growth. Des.* **2017,** *17*, 19-27.

(38) Sekine, A.; Ina, S.; Johmoto, K.; Uekusa, H., Control of the photochromic behavior of cobaloxime complexes with salicylidene-3-aminopyridine and 2-cyanoethyl groups by dual photoisomerization. *CrystEngComm.* **2016,** *18*, 7330-7338.

(39) Marchivie, M.; Guionneau, P.; Howard, J. A. K.; Chastanet, G.; Létard, J.-F.; Goeta, A. E.; Chasseau, D., Structural Characterization of a Photoinduced Molecular Switch. *J. Am. Chem. Soc.* **2002,** *124*, 194-195.

(40) Buron-Le Cointe, M.; Ould Moussa, N.; Trzop, E.; Moréac, A.; Molnar, G.; Toupet, L.; Bousseksou, A.; Létard, J. F.; Matouzenko, G. S., Symmetry breaking and light-induced spin-state trapping in a mononuclear Fe^{II} complex with the two-step thermal conversion. *Phys. Rev. B.* **2010,** *82*, 214106.

(41) M. J. Frisch, G. W. Trucks, H. B. Schlegel, G. E. Scuseria, M. A. Robb, J. R. Cheeseman, G. Scalmani, V. Barone, G. A. Petersson, H. Nakatsuji, X. Li, M. Caricato, A. Marenich, J. Bloino, B. G. Janesko, R. Gomperts, B. Mennucci, H. P. Hratchian, J. V. Ortiz, A. F. Izmaylov, J. L. Sonnenberg, D. Williams-Young, F. Ding, F. Lipparini, F. Egidi, J. Goings, B. Peng, A. Petrone, T. Henderson, D. Ranasinghe, V. G. Zakrzewski, J. Gao, N. Rega, G. Zheng, W. Liang, M. Hada, M. Ehara, K. Toyota, R. Fukuda, J. Hasegawa, M. Ishida, T. Nakajima, Y. Honda, O. Kitao, H. Nakai, T. Vreven, K. Throssell, J. A. Montgomery, Jr., J. E. Peralta, F. Ogliaro, M. Bearpark, J. J. Heyd, E. Brothers, K. N. Kudin, V. N. Staroverov, T. Keith, R. Kobayashi, J. Normand, K. Raghavachari, A. Rendell, J. C. Burant, S. S. Iyengar, J. Tomasi, M. Cossi, J. M. Millam, M. Klene, C. Adamo, R. Cammi, J. W. Ochterski, R. L. Martin, K. Morokuma, O. Farkas, J. B. Foresman, and D. J. Fox. Gaussian 09, Revision E.01, Gaussian, Inc., Wallingford CT, 2016.

(42) Reiher M, Salomon O, Hess B. A. Reparameterization of hybrid functionals based on energy differences of states of different multiplicity. *Theor. Chem. Acc*. **2001,** *107*, 48-55.

(43) Salomon O, Reiher M, Hess B. A. Assertion and validation of the performance of the B3LYP* functional for the first transition metal row and the G2 test set. *J. Chem. Phys.* **2002**, *117*, 4729-4737.

(44) Becke, A. D. Density-functional exchange-energy approximation with correct asymptotic behavior. *Phys. Rev. A.* **1988,** *38*, 3098-3100.

(45) Lee, C; Yang, W; Parr, R. G. Development of the Colle-Salvetti correlation-energy formula into a functional of the electron density. *Phys. Rev. B*. **1988,** *37*, 785-789.

(46) Becke, A. D. Density-functional thermochemistry. III. The role of exact exchange. *J. Chem. Phys.* **1993**, *98*, 5648-5652.

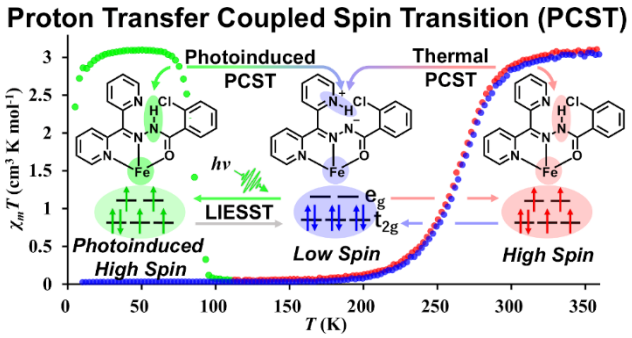
Proton Transfer Coupled Spin Transition (PCST)
Photoinduced
PCST
Thermal
PCST
hν
LIESST
Photoinduced
High Spin
Low Spin
High Spin
e_g
t_{2g}
$\chi_m T$ (cm^3 K mol^{-1})
T (K)

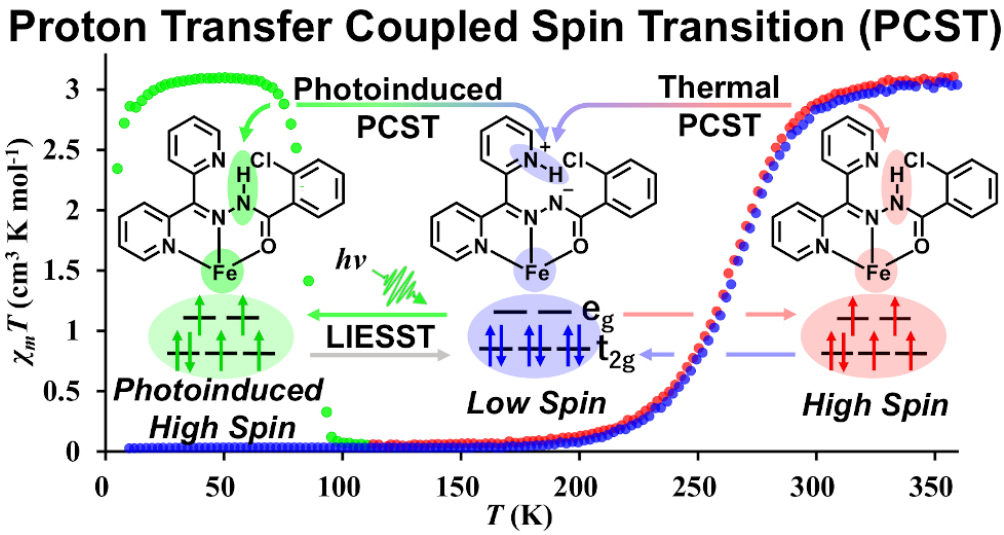

82x44mm (300 x 300 DPI)